Endurance limit of die-cast magnesium alloys AM50hp and AZ91hp depending on type and size of internal cavities

B. Köhler [a,*], H. Bomas [a], W. Leis [b], L. Kallien [b]

[a] Stiftung Institut für Werkstofftechnik, Badgasteiner Straße 3, D-28359 Bremen, Germany
[b] Hochschule Aalen, Beethovenstraße 1, D-73430 Aalen, Germany

ARTICLE INFO

ABSTRACT

The aim of this work was to investigate the influence of internal cavities on the fatigue properties of two of the technical most common die-cast magnesium alloys, AM50hp and AZ91hp. For this purpose the endurance limits of altogether three batches of S–N specimens, two conventional cast and one vacural cast, with varying internal defects have been measured. After fatigue failure the fracture surface of each sample has been analysed with respect to the site of crack initiation and, where appropriate, the size of the crack initiating cavity or pore. Moreover, on both alloys crack growth tests have been carried out and the thresholds ΔK_{th} of the stress intensity factor have been measured.

Finally, the experimental data from both, the S–N tests and the crack propagation measurements, were depicted in a modified Kitagawa–Takahashi diagram. Using El Haddad's and Topper's approach the distribution function of the endurance limit has been proposed, whose parameters could be determined by fitting them to the experimental results. The knowledge of these parameters allows the calculation of the fracture probability as a function of an equivalent crack length and the stress amplitude.

© 2012 Elsevier Ltd. All rights reserved.

1. Introduction

The alloy AZ91 is the most common die-cast magnesium alloy being characterised by high strength, good castability, and high corrosion resistance. In fact, the high strength, investigated at separately cast specimens is often not reached in real components. The reasons for this are an inhomogeneous microstructure, gas inclusions or microvoids. Possible causes for such kinds of inner defects are

- air pockets from the casting set or the die-casting form,
- gases as decomposition products of auxiliary materials,
- shrinkage cavities from the phase transition liquid/solid,
- segregations and
- non-metallic inclusions.

Frequently, porous zones arise during the die-casting process, especially at transitions of wall thickness and areas where force lines are deflected as well. One explanation for this phenomenon given by Dahle and St. John is based on the interaction between externally solidified crystals (ESCs) and newly nucleation at the mould [1]. Investigations by Kinzler et al. indicate shrinkage-induced porosity having an influence on the mechanical behaviour of

AM50hp and AZ91hp at high strain rate [2]. The authors visualise the three-dimensional inhomogeneity distribution and describe its effect on mechanical strength values. A quantitative description of spatial arrangement of shrinkage cavities and gas pores in cast Mg alloys of the AM series is given by Balasundaram and Gokhale [3]. Liu et al. also describe the influence of porosities on mechanical characteristic values of the alloys AZ91hp, AM50hp, AS41, and AE42 [4]. Whereas the yield strength has been found to be practically uninfluenced by porosity, a correlation between tensile strength and ultimate elongation was observed, both depending on the porosity, a fact that also holds for other die-cast alloys [5].

Moreover, for a broad application of die-cast Mg-alloys it is necessary to obtain knowledge about their fatigue behaviour. Investigations on the alloys AZ91hp, AM50hp, and AM20hp were carried out by Sonsino et al. and compared to corresponding data of several steels and Al-alloys [6]. Eisenmeier et al. studied the cyclic deformation and fatigue behaviour of the alloy AZ91 at constant strain amplitudes between 1.4×10^{-3} and 2×10^{-2} at room temperature and at 130 °C [7]. They verified that crack propagation occurs mainly by the coalescence of smaller cracks. Höppel et al. carried out fatigue experiments at AZ91 and point out that for crack initiation cavities at or beneath the surface play an important role [8]. Badini et al. establish a connection between mechanical properties and cast defects in Al and Mg die-cast alloys [9]. The latter emphasise the particular importance of the distribution and morphology of defects as well as their location within casting for

* Corresponding author. Tel.: +49 421 218 51313; fax: +49 421 218 51333.
E-mail address: koehler@iwt-bremen.de (B. Köhler).

Table 1
Chemical composition of the magnesium die-casting alloys AM50hp and AZ91hp.

Alloy	Alloying element (mass%)						
AM50hp	Al	Mn	Zn	Si	Cu	Ni	Fe
	4.5–5.3	0.28–0.5	<0.2	<0.05	<0.008	<0.001	<0.004
AZ91hp	Al	Mn	Zn	Si	Cu	Ni	Others
	8.5–9.5	0.15–0.4	0.45–0.9	<0.02	<0.08	<0.01	<0.30

fatigue properties. Zenner and Renner show, that the results from fatigue examinations at the alloys AZ91 and AM60 are strongly affected by inner defects as microporosity for example [10]. The Mg alloys AZ91, AM60, AE21 and AS21 as well as the Al-alloy AlSi9Cu3 were compared by Mayer et al. with respect to their fatigue behaviour [11]. The experiments have been performed up to 10^9 cycles using an ultrasonic fatigue testing method. At this, the Mg alloys reached endurance limits of 34–55 MPa while the Al alloy showed a mean endurance limit of 75 MPa. In 98.5% of the specimens crack initiation at porosity was observed.

Examinations on die-cast aluminium of Linder et al. focused on the fatigue strength assessments of differently sized defects in terms of a Kitagawa diagram, which can be used to prescribe the largest allowable defect at a given load situation [12]. Similar investigations on die-cast aluminium were carried out by Oberwinkler et al. who derive the sustainable local load by combining the results of a statistical porosity model and the Kitagawa diagram [13].

In this investigation two of the most commonly used magnesium die-casting alloys, AZ91hp with main alloying elements aluminium and zinc and AM50hp with main alloying elements aluminium and manganese have been studied. For reasons deriving from corrosion protection today's alloys are of high purity (hp), having very low contents of iron, nickel and copper. In order to study the influence of typical die-casting caused microporosity on fatigue behaviour three sample batches have been investigated. Therefore different types of pores have been inserted by variation of the die-cast parameters within the same batch. In contrast to most other studies the fatigue behaviour of the specimens has been tested directly without removing the casting skin, so equalling a real component's surface. Finally, the fracture surfaces have been

analysed. Thereby defect induced failure could be interpreted by a Kitagawa analysis to derive the influence of defect size and stress amplitude on the number of cycles to failure [14].

2. Material

In the present investigation the most frequently used die-cast magnesium alloys AM50hp and AZ91hp were chosen as materials of study. While AZ91hp excels in its high strength and good corrosion resistance, AM50hp is attractive for its ductility. The chemical composition of both materials is shown in Table 1.

3. Experimental procedure

3.1. Die-casting

For the manufacturing of the specimens a specially constructed die-casting mould was built, which included two fatigue specimens and two plate-like samples (250 mm × 60 mm) for fracture mechanics experiments with each of them having 2 and 6 mm wall thickness. It had been optimised performing simulations of the solidification in the run-up (Fig. 1) resulting in a mould that is well suited for conventional die-casting as well as for vacural die-casting (Fig. 2). The latter is characterised by evacuating the mould before it is entered by the melt, so that entrapped air as well as an oxidation of the melt is suppressed widely.

The casting was carried out at a 7.5 MN die-casting machine in conventional and vacural process. In order to generate specimens including different configurations of inner defects with respect to size, type and distribution, the process parameters prefilling velocity v_1, plunger velocity v_2 and casting pressure p have been varied within the same batch in certain limits:

- v_1 = 0.4–0.8 m/s,
- v_2 = 2.0–3.5 m/s and
- p = 5×10^7–1×10^8 Pa.

To avoid results being influenced negatively by run-up conditions at least the first five castings of every specimen series with the same set of parameters have been rejected.
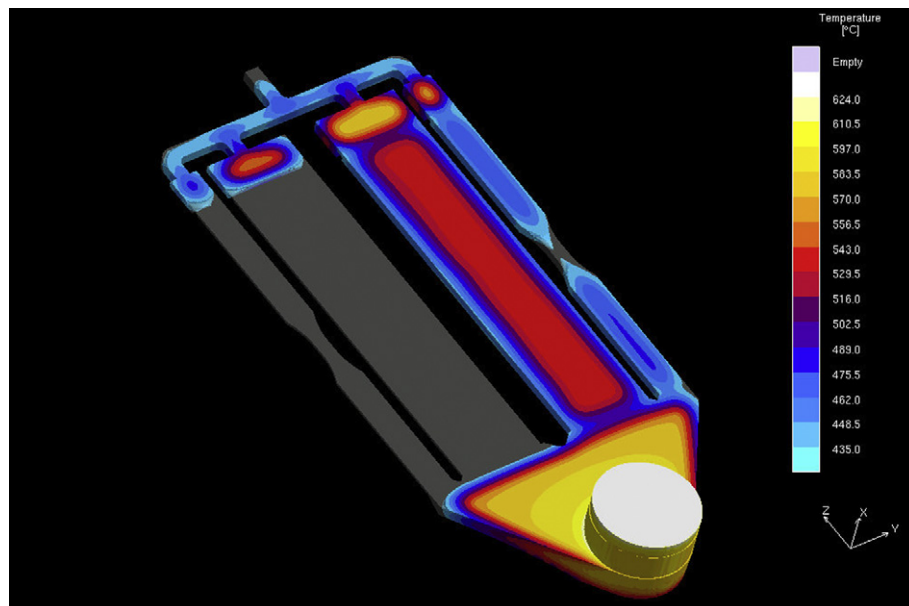

Fig. 1. Simulation of temperature during the solidification of the cast: In contrast to the completely solidified two specimens on the left hand with 2 mm wall thickness, the two specimens on the right with 6 mm wall thickness contain liquid parts. This means that the right hand side cannot be fed sufficiently and shrinkage porosity arises.

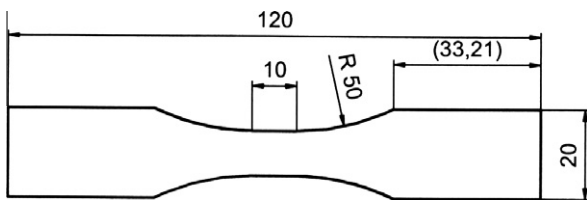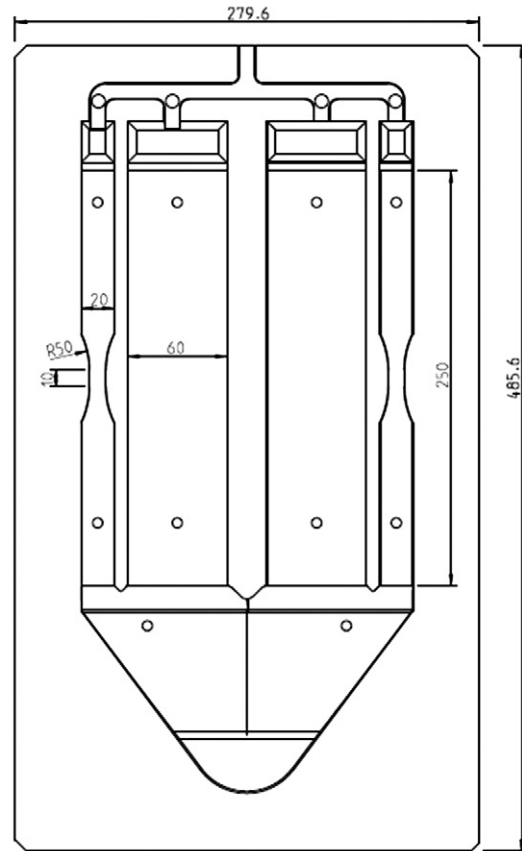**Fig. 2.** Die-casting mould for tensile specimens and plate-like samples.

Fig. 3. Directly cast flat tensile specimen for fatigue tests, thickness = 6 mm.

3.2. Pulsating tensile tests

Altogether three batches of die-cast Mg alloys have been tested in pulsating tensile tests at a stress ratio $R = 0.1$: AM91hp, die-cast in conventional and vacural process and AM50hp, conventionally die-cast. Each batch included specimens cast with different process parameters v_1, v_2 and p, hence varying configurations of inner defects such as pores or cavities. The specimens had a thickness of 6 mm and have been tested as-cast, this means without scale removal retaining near net shape surface finish (Fig. 3). The fatigue tests were performed at a resonance testing machine at a frequency of 80 Hz till sample's fracture or 10^7 load reversals (Fig. 4). In order to determine the endurance limit σ_D, for every of the three batches an S–N diagram was generated with at least four stress amplitudes σ_a between 35 and 55 MPa. The fracture surfaces of all failed specimens were investigated with scanning electron microscopy (SEM) in order to localise the site and origin of crack initiation. If the crack was initiated at an inner cavity such as a pore or a blowhole, the defect's area in the fracture plane has been measured with the aid of the software ImageJ. In order to identify the potential crack initiating defect in the run outs, they

have been tested once more at increased stress amplitudes up to the point of rupture. Afterwards the fracture surface was analysed in the same manner as mentioned above.

3.3. Crack growth rate measurements

Due to the striven Kitagawa analysis it is necessary to determine the threshold of the stress intensity factor ΔK_{th} for both alloys. In order to determine these values the fatigue crack growth rate has been measured using a compact-tension specimen machined from the plate-like blanks (Fig. 2) according to ASTM E 647 (Fig. 5).The specimens were manufactured from the plate bodies which have been die-cast simultaneously with the fatigue-test specimen (Fig. 2). To ensure studying crack propagation on samples being free as possible of casting defects or internal cavities, samples were chosen on the basis of computer tomographical scans. In contrast to the tension fatigue test specimens the skin was removed by milling. To ensure an optimal observability of the crack growth with measuring microscopes, the sample has been polished in the middle section after a Chevron-notch had been inserted. Furthermore, strain gauges on the front and on the specimens' rear side were applied to have control about a possible bending while the sample is getting clamped. At the beginning of every measurement the specimens were cyclically loaded at constant stress amplitude and stress ratio $R = 0.1$ until a fatigue precrack of the order of 1–2 mm had formed. Keeping the stress ratio constant the stress amplitude has been lowered stepwise. The investigations were carried out in strong alignment with ASTM E 647 [15]. A detailed description of the procedure, based on optical observation of the crack propagation, can be found at Taylor [16,17]. At every stress amplitude the crack growth was measured
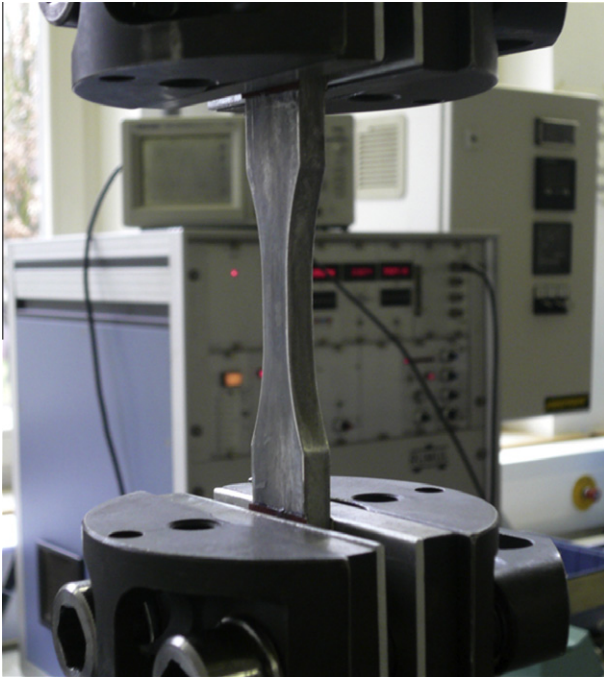
Fig. 4. As-cast fatigue specimen in the clamping device of the resonance testing machine.

Fig. 6. S–N-curves (● fracture, ○ run out).

light-microscopically with a resolution q of about 1×10^{-5} m on the front and rear of the specimen as well to control the symmetry of crack propagation. The criterion $|a_{front} - a_{rear}|/W \leqslant 0.25$ has always been fulfilled, whereby W is the width of the sample, a_{front} is the crack length on the front of the sample and a_{rear} the one on the rear. The common criterion for crack arrest is, if at a given stress amplitude after $q/10^{-11}$ cycles crack growth is no longer visible. Taking a resolution of $q = 1 \times 10^{-5}$ m as a basis, this period results to be 1×10^{6} cycles in these examinations.

4. Experimental results

4.1. Tensile endurance limit

Basically the fatigue strength would be expected to be clearly influenced by inner defects, which should cause notch or crack effects and result in localised stress build-ups. For example, under pressure enclosed gas should cause a complex distribution of inner
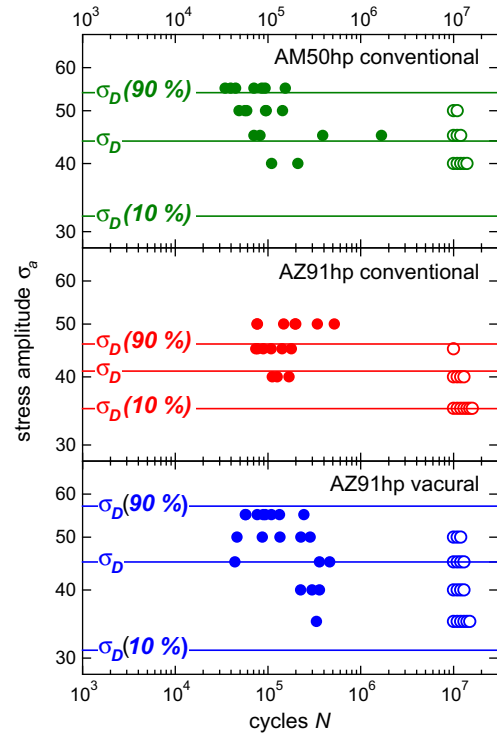
material stresses. Thinking of this, vacural die-casting should decrease number and size of such inner defects, causing an increase of fatigue strength.

The results of the fatigue tests are shown in S–N diagrams in Fig. 6. For each batch which is defined by a certain combination of casting parameters at least seven specimens at four different stress amplitudes have been tested. It was assumed that the endurance limit follows a two-parametric Weibull distribution, which can be written in the form proposed by Bomas et al. [18]:

$$P_f = 1 - 2^{-\left(\frac{\sigma_a}{\sigma_D}\right)^m} \tag{1}$$

At this the median of the endurance limit σ_D and the Weibull exponent m are free parameters which can be fitted to experimental data using the least square method. Moreover, the 10% and 90% quantiles can be calculated from m and σ_D inserting the corresponding failure probabilities into Eq. (1):
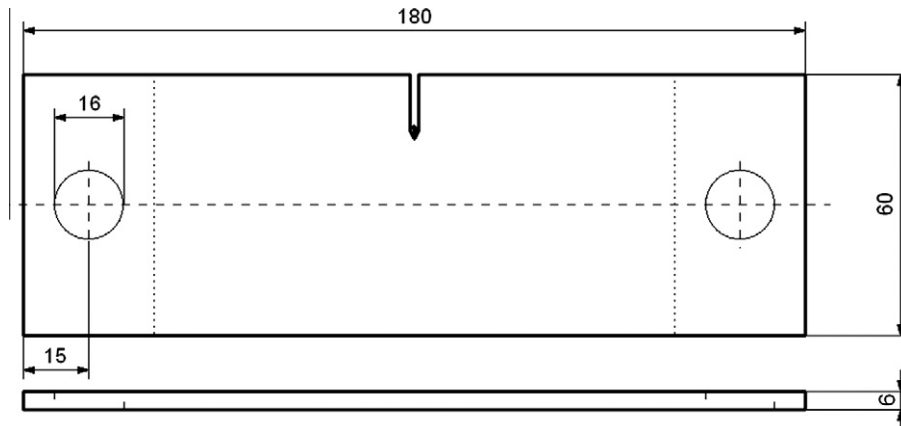

Fig. 5. Compact-tension specimen following ASTM E 647, $W = 60$ mm, $t = 6$ mm [15].

Table 2
Endurance limit at stress ratio $R = 0.1$.

	AM50hp	AZ91hp	
	Conventional	Vacural	Conventional
σ_D (10%) (MPa)	32	31	35
σ_D (MPa)	44	45	41
σ_D (90%) (MPa)	54	57	46
T_σ	1:1.7	1:1.8	1:1.3
m	6	5	11

$$0.1 = 1 - 2^{-\left(\frac{\sigma_D(10\%)}{\sigma_D}\right)^m} \quad \text{and} \quad 0.9 = 1 - 2^{-\left(\frac{\sigma_D(90\,\%)}{\sigma_D}\right)^m} \tag{2}$$

Solving these equations for the quantiles $\sigma_D(10\%)$ and $\sigma_D(90\%)$ leads to:

$$\sigma_D(10\%) = \sqrt[m]{-\ln 0.9 / \ln 2} \cdot \sigma_D \quad \text{and}$$

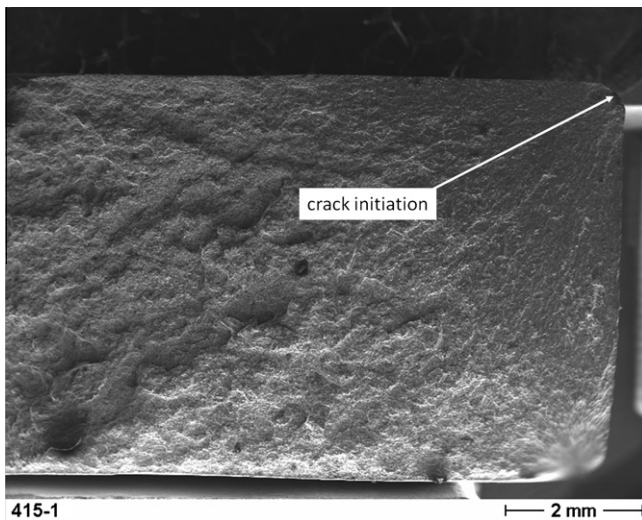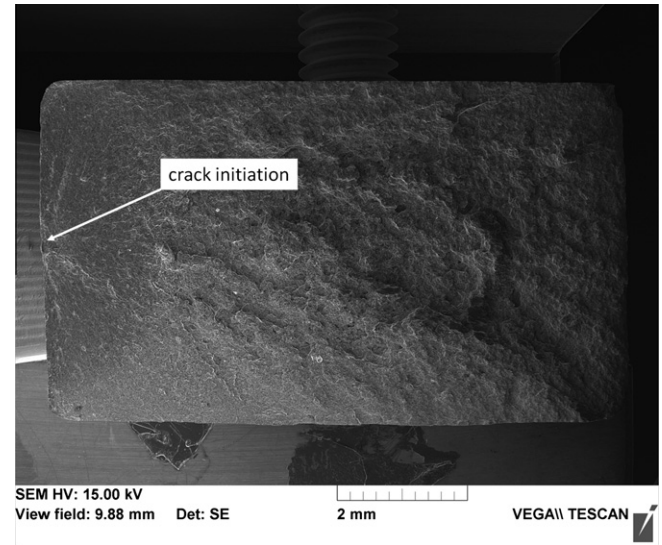$$\sigma_D(90\%) = \sqrt[m]{-\ln 0.1 / \ln 2} \cdot \sigma_D \tag{3}$$

An overview of the fatigue results is given in Table 2, whereby the scatter of the endurance limit is described by the spread $T_\sigma = \sigma_D(10\%)/\sigma_D(90\%)$.

Compared with conventionally die-cast AZ91hp, the endurance limit of the corresponding die-cast AM50hp is slightly increased. The vacural cast batch of AZ91hp surprisingly shows only a small increase of about 4 MPa in endurance limit against the conventional processed batch. Within the maximal permissible error all three endurance limits can be considered to be nearly the same.

4.2. Fracture surface analysis

The analysis of the fracture surfaces with SEM revealed the following sites of crack initiation: surface failure, such as crack initiation at the edges or the side surfaces of the sample, or volume failure, as crack formation at pores or shrinkage cavities. Two examples for the former are given exemplarily in Figs. 7 and 8 while Fig. 9 shows a failure caused by crack initiation at a shrinkage cavity. In contrast to this, crack formation at a pore, as the second type of volume defect, is shown in Fig. 10. A summary of the complete data of the samples represented in Figs. 7–10 is given in Table 3.

A summary of all crack initiation sites is shown in Table 4. Obviously nearly in half of the specimens the failures are initiated in the

Fig. 8. Crack initiation at the side surface of a sample.
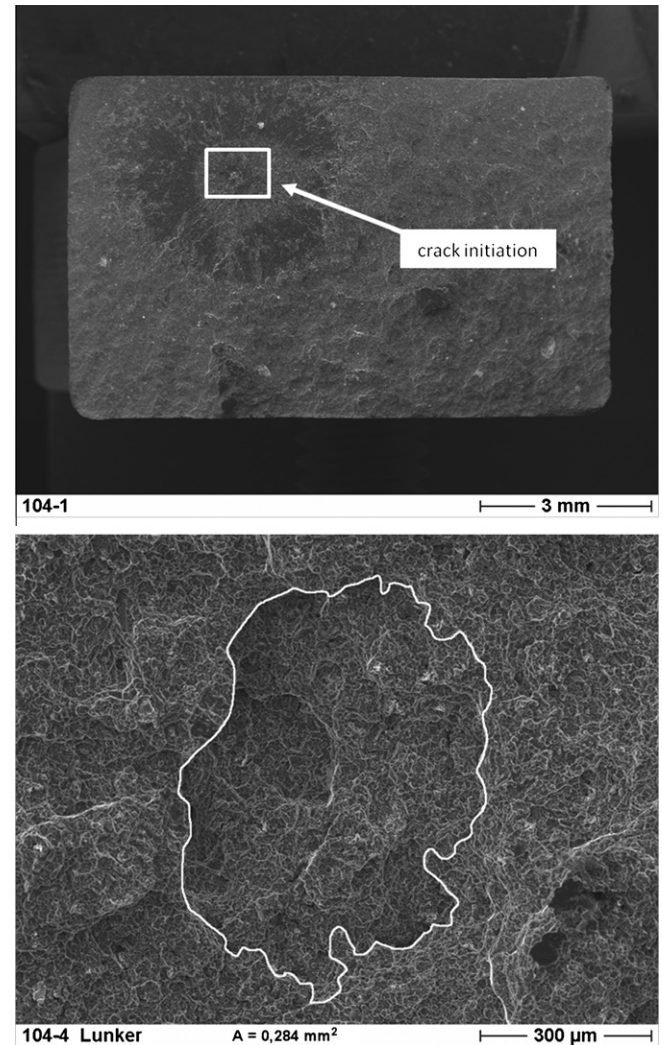
Fig. 9. Crack initiation at a cavity: Overview of the fracture plane of a conventional die-cast AZ91hp specimen (top), partial enlargement of the cavity with traced outline, projected area $A = 0.284$ mm^2 (bottom).

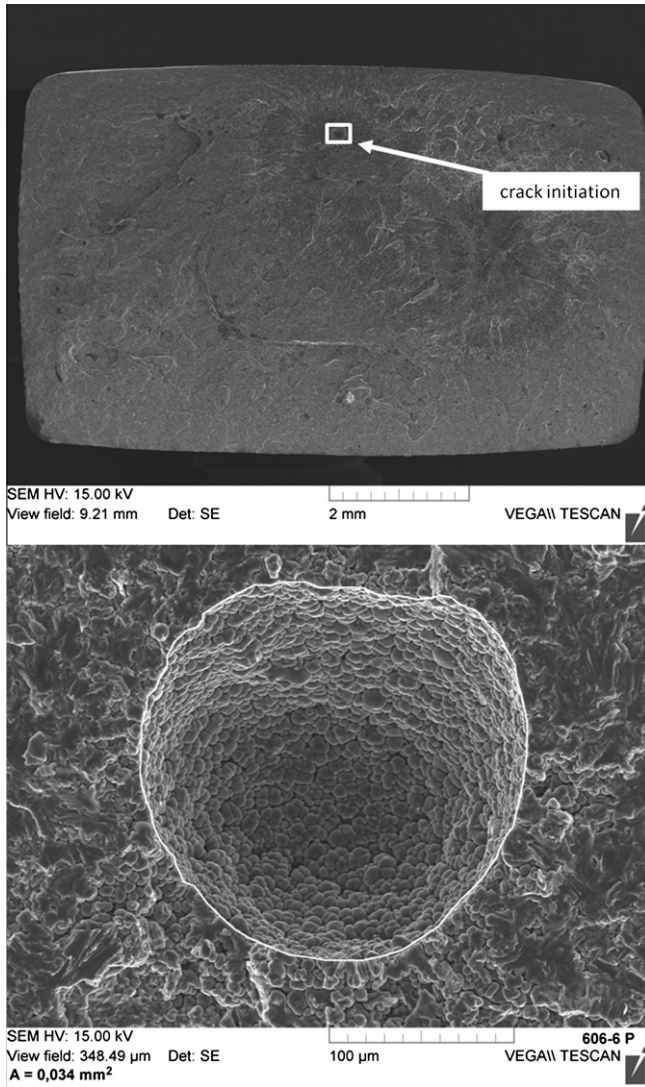**Fig. 7.** Crack initiation at the edge of a sample.

Fig. 10. Crack initiation at a pore: overview of the fracture plane of a vacural die-cast AZ91hp specimen (top), partial enlargement of the pore with traced border, projected area $A = 0.034$ mm^2 (bottom).

surface planes or at the edges. This might be due to the defective, unpolished, as-cast surface of the samples. At the remaining specimens volume failure has been observed, whereby the prevailing crack initiation took place at cavities. Merely the conventional die-cast AM50hp alloy showed a balanced relation between crack formation at cavities and at pores.

Regarding to the Kitagawa analysis (see Section 4.4) all crack initiating volume defects were magnified and their projection onto the fracture plane was measured to classify the size of the defects. Moreover fracture mechanics investigations were carried out to determine the thresholds of the stress intensity factor ΔK_{th} and to get information about crack propagation within the range of Linear Elastic Fracture Mechanics (LEFM).

Table 4
Summary of crack initiation sites.

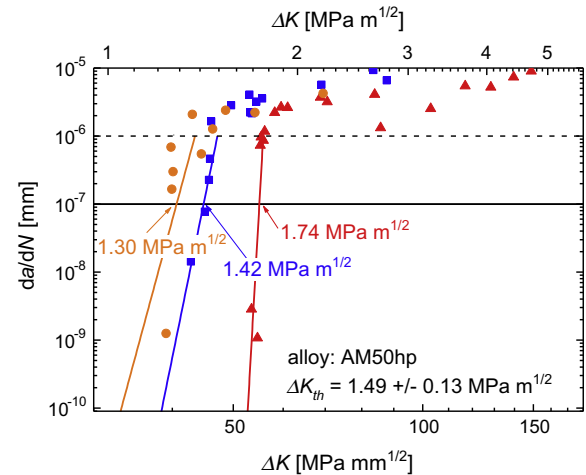| Alloy	Casting process	Number of crack initiations at:			
		Cavity	Pore	Surface	Edge
AM50hp	Conventional	7	7	2	21
AZ91hp	Conventional	10	2	2	6
	Vacural	11	1	1	1
Sum		28	10	5	28
Volume failure ⇔ surface failure		38 (=54%)		33 (=46%)	

Fig. 11. Determination of the threshold of the stress intensity factor ΔK_{th} for the alloy AM50hp (die-casting parameters: $v_1 = 0.8$ m/s; $v_2 = 2$ m/s; $p = 1 \times 10^8$ Pa, vacural).

4.3. Threshold of fatigue crack propagation

The stress intensity factor K depends on the crack length a and the applied tensile stress σ and results to

$$K = \sigma\sqrt{\pi a} \cdot Y(\alpha) \tag{4}$$

whereby

$$Y(\alpha) = 1.12 - 0.231\alpha + 10.55\alpha^2 - 21.72\alpha^3 + 30.39\alpha^4 \tag{5}$$

is a geometry factor with $\alpha = a/W$, $a = (a_{front} + a_{rear})/2$, the specimens' width W and the crack length on the front a_{front} and on the rear a_{rear} [19]. It follows the term for the stress range of the stress intensity factor:

$$\Delta K = K_{max} - K_{min} = \frac{F_{max} - F_{min}}{W \cdot t}\sqrt{\pi a} \cdot Y(\alpha) \tag{6}$$

with maximum force F_{max}, minimum force F_{min} and the specimens' thickness t.

Cyclic crack propagation was observed at three specimens for each alloy (Figs. 11 and 12) complying with ASTM E 647 standard. Starting in the Paris-law region, at a crack propagation rate of $da/dN = 10^{-5}$–10^{-6} mm, the crack growth has been studied with stepwise load shedding towards decreasing growth rate. Below crack propagation rates of 10^{-6} mm the curve deviates from

Table 3
Die-casting and fatigue data of the specimens in Figs. 7–10.

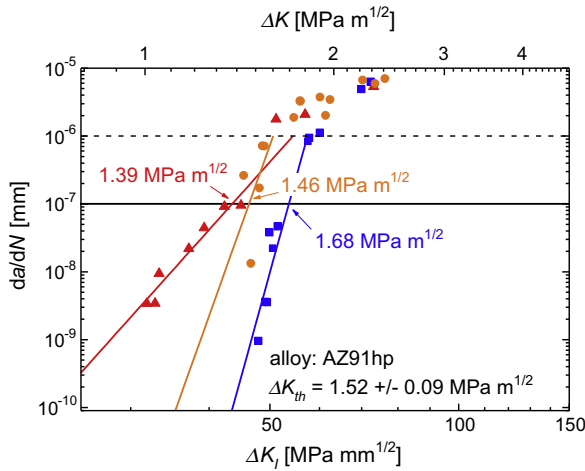| Fig.	Spec. No.	Alloy	Casting process	v_1 (m/s)	v_2 (m/s)	p (10^5 Pa)	Failure	σ_a (MPa)	N_f
7	415	AM50hp	Conventional	0.4	2	1000	Edge	52	53,300
8	507	AZ91hp	Vacural	0.4	2	1000	Surface	52	68,000
9	104	AZ91hp	Conventional	0.4	3.5	500	Cavity	50	215,700
10	606	AZ91hp	Vacural	0.4	2	1000	Pore	50	134,500

Fig. 12. Determination of the threshold of the stress intensity factor ΔK_{th} for the alloy AZ91hp (die-casting parameters: $v_1 = 0.4$ m/s; $v_2 = 3.5$ m/s; $p = 1 \times 10^8$ Pa, vacural).

Table 5
Results of crack propagation measurements and comparison with literature data.

Alloy	$\Delta K_{I\,th}$ (MPa m$^{1/2}$)	
	These studies	Literature data [11,20]
AM50hp	1.49 ± 0.13	–
AM60hp	–	1.40–1.55
AZ91hp	1.52 ± 0.09	1.30–1.55

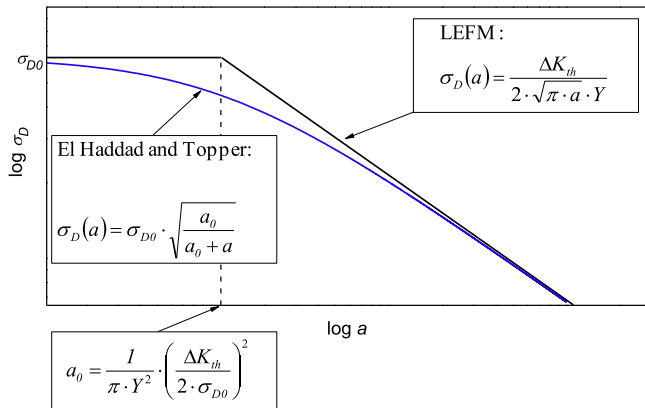**Fig. 13.** Kitagawa diagram with approach of El Haddad and Topper, describing the influence of long and short cracks on the endurance limit σ_D.

Paris-law behaviour and goes to the threshold value of the stress intensity factor ΔK_{th} at a crack growth rate of $da/dN = 10^{-7}$ mm, below which propagation effectively ceases. The determination of ΔK_{th} is achieved by linear interpolation on $da/dN = 10^{-7}$ mm of at least five measured values from the range $da/dN < 10^{-6}$ mm [15]. It is notable that for both alloys the scatter near the threshold region seems to be rather large. This is due cast defects which may stop the crack propagation, for example if the crack tip meets a cavity. In this case the range of the stress intensity factor ΔK had to be slightly increased till the crack tip overcame the defect and crack propagation continued. In fact, despite careful selection of the crack propagation specimens based on computer tomographical scans, such casting defects are not completely avoidable.

In Table 5 the mean values of ΔK_{th} resulting from the three measurements on both alloys shown in Figs. 11 and 12 are set

against literature data [11,20]. In the absence of a reference value for the alloy AM50hp, the very similar die-cast alloy AM60hp has been chosen. Obviously the experimental results of this study and literature values are in good agreement.

4.4. Evaluation of the endurance limit based on the Kitagawa–Takahashi approach

The influence of microscopic and macroscopic cracks of the length a on the endurance limit σ_D can be described within the Kitagawa diagram (Fig. 13) [14]. The area of short cracks is delimited from the range of Linear Elastic Fracture Mechanics (LEFMs) by a characteristic crack length

$$a_0 = \frac{1}{\pi Y^2} \cdot \left(\frac{\Delta K_{th}}{2 \cdot \sigma_{D0}} \right)^2 \tag{7}$$

σ_{D0} is the endurance limit of a specimen without cracks and Y is the geometry factor of the crack. In the simplest case, if a circular internal crack in infinite neighbourhood ("pennyshaped crack") is assumed, the geometry factor arises to $Y = 2/\pi$ [21].

The Kitagawa–Takahashi approach has been modified by El Haddad and Topper [22] describing the endurance limit depending on a as

$$\sigma_D(a) = \sigma_{D0} \cdot \sqrt{\frac{a_0}{a_0 + a}} \tag{8}$$

In order to verify that Kitagawa's model gives an adequate description within these investigations, at first the results of the fracture surface analyses on the σ–N specimens were used. From the size of the crack initiating defect, measured as the area projected onto the fracture plane, a defect size with a dimension of a length can be calculated using the approach of Murakami [23] taking the penny shape of the crack into account additionally:

$$a = \sqrt{\frac{area}{\pi}} \tag{9}$$

This defect size a, interpreted in terms of a crack length, can be plotted in a Kitagawa diagram (Fig. 14, filled circles). Additionally, the most dangerous defects in the run outs have been identified. For this purpose the amplitude σ_a of these specimens has been increased gradually till failure occurred. Afterwards a fracture surface analysis as stated above took place, permitting to present the run outs with their most dangerous defects in the Kitagawa diagram (Fig. 14, open circles) as well. A second set of experimental data can be extracted from the investigations of crack propagation (see Section 4.3). At every measured point here a stress amplitude σ_a has been applied to a compact-tension specimen with a crack of a known length a, observing the crack propagation rate da/dN. According to ASTM E 647 a crack growth rate of $da/dN < 10^{-7}$ is interpreted as crack stop, which means at the applied load no failure occurs and this result can be valued as a run out (Fig. 14, open triangles). If on the other hand crack growth rates of $da/dN \geqslant 10^{-7}$ are observed, crack propagation occurs and the specimen will fail (Fig. 14, filled triangles).

In order to depict the experimental results of the fracture surface analysis and of the crack propagation measurements in the same Kitagawa–Takahashi diagram, it is necessary to consider the different geometry factors of the penny-shaped crack $Y = 2/\pi$ and of the crack in the compact-tension specimen $Y(\alpha)$ (see Eq. (5)). For this purpose it is useful to introduce an "equivalent crack length"

$$a_{eq} = aY^2 \tag{10}$$

including the geometry factor Y. A simple calculation leads to the transformation of Eqs. (7) and (8), describing El Haddad's and Top-
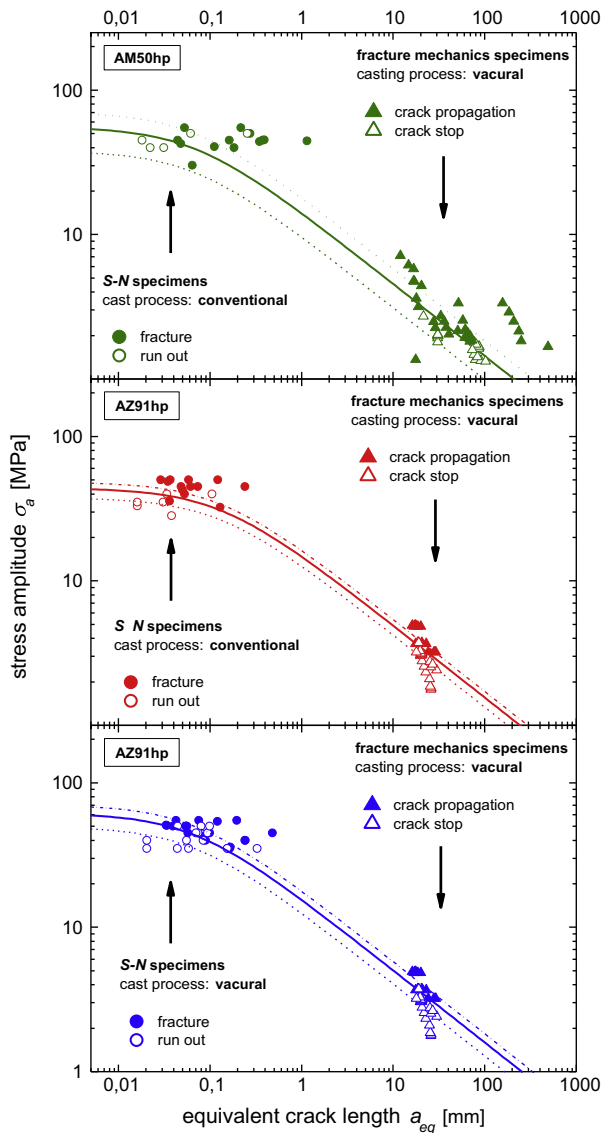
Fig. 14. Kitagawa–Takahashi diagrams for the three investigated batches based on experimental data from the fracture surface analyses of the σ–N specimens and from the crack propagation investigations. Contour lines for three fracture probabilities calculated on the approach of El Haddad and Topper are drawn for P_f = 0.1 (dashed line), 0.5 (solid line) and 0.9 (dotted line).
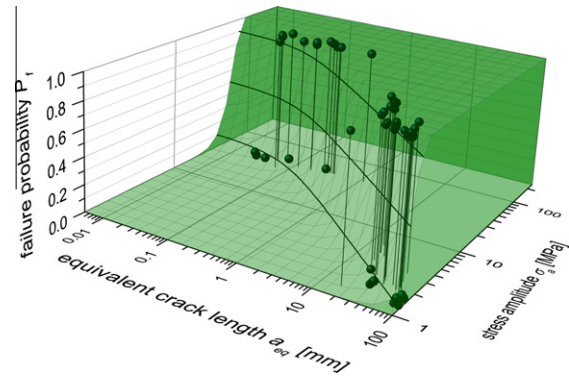

Fig. 15. Three-dimensional Kitagawa–Takahashi diagram for conventionally cast alloy AM50hp with experimental data (balls without anchor lines = run outs respectively crack stop, balls with anchor lines = fracture respectively crack growth) and fitted probability plane based on a two-parametric Weibull distribution of the endurance limit.

The Kitagawa–Takahashi diagram shows the endurance limit of a crack-bearing part as a function of the crack length. Knowing that the endurance limit is a random variable, a statistical interpretation of the diagram is possible saying that the El-Haddad-Topper curve shows the course of the median of the endurance limit. With this idea, the diagram represents a cutting plane in a three-dimensional diagram, namely the graphical representation of the distribution function $F_{\text{endurance limit}}$ (a_{eq}, σ_a) depending on the crack size a_{eq} and the stress amplitude σ_a. Replacing the median σ_D with the help of Eq. (11) shows the dependence of the distribution function on the equivalent crack length:

$$F_{\text{endurance limit}}(a_{eq}, \sigma_a) = 1 - 2^{\left(\frac{\sigma_a}{\sigma_{D0}}\right)^m \cdot \left(1 + \frac{a_{eq}}{a_{0eq}}\right)^{m/2}} \tag{13}$$

According to its mathematical definition the distribution function of the endurance limit at the stress amplitude σ_a is the probability that the endurance limit is smaller than the stress amplitude:

$$F_{\text{endurance limit}}(a_{eq}, \sigma_a) = P \text{ (endurance limit at } a_{eq} < \sigma_a) \tag{14}$$

The physical sense of the event "endurance limit at $a_{eq} < \sigma_a$" is failure or fracture before the specimen reaches 10^7 cycles. This means that the distribution function of the endurance limit is the probability of fracture:

$$F_{\text{endurance limit}}(a_{eq}, \sigma_a) = P_f(a_{eq}, \sigma_a) \tag{15}$$

These fracture probabilities with the sizes of the corresponding crack initiating or most dangerous defects and the applied stress amplitudes are available for all tested specimens being P_f (a_{eq}, σ_a) = 1 for the broken specimens and the compact-tension specimens with da/dN > 10^{-7} mm and P_f (a_{eq}, σ_a) = 0 for the run out specimens and the compact-tension specimens with da/dN < 10^{-7} mm. They are visible in the diagrams as filled or open circles for the σ–N specimens and as filled or open triangles for the fracture mechanics specimens as well (Fig. 14). These data sets are the basis for the calculation of the best fitting model parameters σ_{D0}, a_{0eq} and

per's approach of the endurance limit depending on the equivalent crack length:

$$\sigma_D(a_{eq}) = \sigma_{D0} \cdot \sqrt{\frac{a_{0eq}}{a_{0eq} + a_{eq}}} \tag{11}$$

with

$$a_{0eq} = \frac{1}{\pi} \cdot \left(\frac{\Delta K_{th}}{2 \cdot \sigma_{D0}}\right)^2 \tag{12}$$

Table 6
Model parameters describing the three-dimensional Kitagawa–Takahashi diagrams.

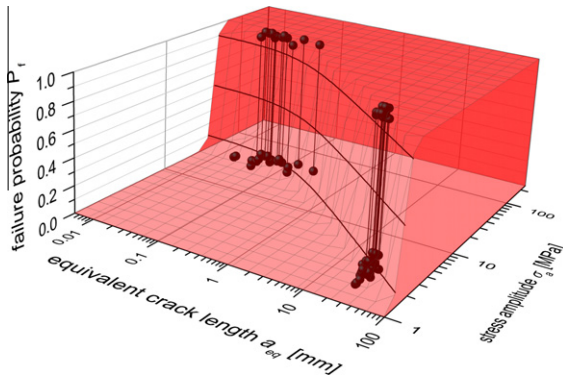| Alloy	Casting process	R	Best fitting model parameters:		
			σ_{D0} (MPa)	a_{0eq} (μm)	m
AM50hp	Conventional	0.1	49	86	5.1
AZ91hp	Conventional	0.1	44	126	12.3
AZ91hp	Vacural	0.1	62	67	8.7

Fig. 16. Three-dimensional Kitagawa–Takahashi diagram for conventionally cast alloy AZ91hp with experimental data (balls without anchor lines = run outs respectively crack stop, balls with anchor lines = fracture respectively crack growth) and fitted probability plane based on a two-parametric Weibull distribution of the endurance limit.

Fig. 17. Three-dimensional Kitagawa–Takahashi diagram for vacural cast alloy AZ91hp with experimental data (balls without anchor lines = run outs respectively crack stop, balls with anchor lines = fracture respectively crack growth) and fitted probability plane based on a two-parametric Weibull distribution of the endurance limit.
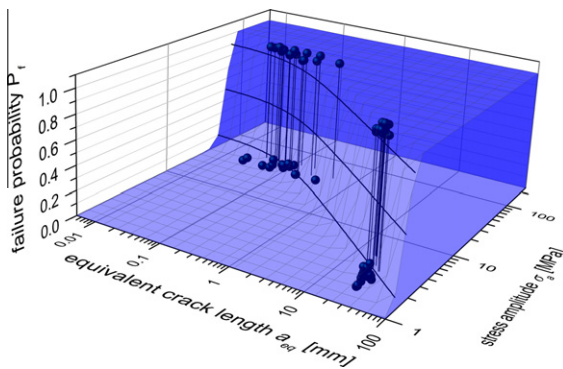
m (Table 6), which have been found using the least square method applied to the sum of the squares $(F_{\text{endurance limit}}(a_i, \sigma_{ai}) - P_f(a_i, \sigma_{ai}))^2$ where the index i indicates the number of the specimen. According to these calculations the contour lines for P_f = 0.1, 0.5 and 0.9 are drawn in the Kitagawa–Takahashi diagrams (Fig. 14).

For vacural AZ91hp it is conspicuous that the sinistral endurance limit σ_{D0} = 62 MPa is considerably different from the measured one σ_D = 45 MPa (Table 2). Consequently, the Kitagawa–Takahashi diagram indicates that the endurance limit of the vacural material could be markedly increased, if casting defects could be avoided. Nevertheless the tested specimens have those defects whereas σ_{D0} describes the endurance limit of the defect-free material. So it is not astonishing that there is a certain gap between the endurance limit of tested specimens and that of the defect-free material.

It is also visible in Fig. 14 that the scatter of the defect sizes increases following the sequence AZ91hp conventional, AZ91hp vacural and AM50hp conventional. Accordingly the shape parameters of the calculated endurance limit distribution functions decrease in this sequence.

Knowing the parameters σ_{D0}, a_{0eq} and m, the distribution function (Eq. (13)) enables the depiction of the failure probability P_f depending on the stress amplitude σ_a and the equivalent crack length a_{eq} as a plane in a three-dimensional diagram (Figs. 15–17).

5. Conclusions

Cyclic tensile tests ($R = 0.1$) on three batches of die-cast magnesium alloys have been carried out on specimens with component-like surfaces, that means without prior scale removal. At this the conventional die cast AM50hp and AZ91hp alloys exhibit endurance limits of σ_D = 44 MPa and 41 MPa, respectively. By comparison to the conventional cast batch of AZ91hp, a simultaneously tested vacural cast batch shows only a slight increase of endurance limit to 45 MPa. The fracture surface analysis shows that nearly half of the fatigue cracks were initiated at the specimens' surface. Thus, in this case the expected advantage of the vacural process with respect to the fatigue strength seems to be of low quantity.

All fatal volume defects such as cavities and pores have been analysed and measured by means of fracture surface analysis at the failed specimens and at the run outs as well. In the latter the stress amplitude σ_a has been increased stepwise starting at the run out level till failure occurred and hence the more dangerous defect could be localised.

Fracture mechanics tests have been carried out on compact tension specimens with nearly no casting defects. The thresholds of the stress intensity factor resulted in ΔK_{th} = 47 MPa mm$^{1/2}$ for AM50hp and ΔK_{th} = 48 MPa mm$^{1/2}$ for AZ91hp.

Both, the results of the fracture surface analysis from the S–N samples and those of the crack growth investigations can be included in one and the same Kitagawa–Takahashi diagram by eliminating the influence of the different crack geometries substituting the defect size a by an equivalent defect size $a_{eq} = a \, Y^{.2}$.

Based on the experimental data from the S–N experiments and the crack growth tests within the range of LEFM on the one hand, and the probability of fracture P_f, described by the distribution function of the endurance limit $F_{\text{endurance limit}}(a_{eq}, \sigma_a)$, on the other hand, it is possible to find the model parameters a_{0eq}, σ_{D0} and m of the distribution function using the least square method. Hence the knowledge of these parameters enables the calculation of a fracture probability at each point of the plane spanned by the stress amplitude axis and equivalent crack length axis of a three-dimensional Kitagawa–Takahashi diagram.

Acknowledgement

References

[1] Dahle AK, John D H St. Die Ursachen von streifenförmigen Fehlern in Magnesiumdruckgussteilen (The causes of ribbon defects in magnesium die-castings). Giesserei-Praxis 2001;7:284–90.
[2] Kinzler T, Pfeifer-Schäller I, Klein F. Influence of temperature and deformation rate on mechanical characteristics of the mg-alloys AZ91 HP and AM50 HP. Konstruktion 2000;52:37–41.
[3] Balasundaram A, Gokhale AM. Quantitative characterization of spatial arrangement of shrinkage and gas (air) pores in cast magnesium alloys. Mater Charact 2001;46:419–26.
[4] Liu Z, Chen L, Zhao H, Wang Y, Klein F. The influence of porosity of magnesium die-casting alloys on its mechanical properties. Metall – Internationale Fachzeitschrift für Metallurgie 2000;54:122.
[5] Bomas H, Grauerholz P, Mayr P. Verhalten von Flachproben aus GD-AlSi8Cu3 unter Zug- und Zugschwellbeanspruchung. Aluminium 1988;64:524–7.
[6] Sonsino CM, Dieterich K, Wenk L, Till A. Fatigue design with cast magnesium alloys. In: Kainer KU, editor. Magnesium alloys and their applications. Weinheim: Wiley VCH; 2000. p. 304–11.
[7] Eisenmeier G, Holzwarth B, Höppel HW, Mughrabi H. Cyclic deformation and fatigue behavior of the magnesium alloy AZ91. Mat Sci Eng A 2001;319–321:578–82.
[8] Höppel HW, Eisenmeier G, Holzwarth B, Mughrabi H. Cyclic deformation behavior of the cast magnesium alloy AZ97. In: Kainer KU, editor. Magnesium alloys and their applications. Weinheim: Wiley VCH; 2000. p. 348–53.

[9] Badini C, Bonollo F, Cavatorta MP, La Vecchia GM, Panvini A, Pola A, et al. Process simulation of microstructure and relationship with mechanical properties in diecastings. Metall Sci Technol 2002;20:14–21.

[10] Renner F, Zenner H. Fatigue strength of die-cast magnesium components. Fatigue Fract Eng Mater Struct 2002;25:1157–68.

[11] Mayer H, Papakyriacou M, Zettl B, Stanzl-Tschegg SE. Influence of porosity on the fatigue limit of die-cast magnesium and aluminium alloys. Int. J. Fatigue 2003;25:245–56.

[12] Linder J, Arvidsson A, Kron J. The influence of porosity on the fatigue strength of high-pressure die cast aluminium. Fatigue Fract Eng Mater Struct 2006;29:357–63.

[13] Oberwinkler Ch, Leitner H, Eichlseder W, Schönfeld F, Schmidt S. Schädigungstolerante Auslegung von Aluminium-Druckgusskomponenten. Mater Test 2010;52(7–8):513–9.

[14] Kitagawa H, Takahashi S. Applicability of fracture mechanics to very small cracks or the cracks in the early stages. In: Proceedings of the second international conference no mechanical behavior of materials. Metals Park, OH: American Society for Metals; 1976. p. 627–31.

[15] Standard test method for measurement of fatigue crack growth rates, ASTM E 647-95a, ASTM; 1995.

[16] Taylor D. Fatigue thresholds. London: Butterworth & Co. Ltd.; 1989.

[17] Taylor D. A Compendium of fatigue thresholds and growth rates. Cradley Heath: Engineering Materials Advisory Services Ltd.; 1985.

[18] Bomas H, Linkewitz T, Mayr P. Application of a weakest-link concept to the fatigue limit of the bearing steal SAE 52100 in a bainitic condition. Fatigue Fract Eng Mater Struct 1999;22:733–41.

[19] Brown WF, Strawley JE. Current status of plain strain toughness testing of high strength metallic materials. ASTM STP 1966;410:12.

[20] Mayer H, Papakyriacou M, Zettl B, Vacic S. Endurance limit and threshold stress intensity of die-cast magnesium and aluminium alloys at elevated temperatures. Int J Fatigue 2005;27:1076–88.

[21] Sommer E. Bruchmechanische Bewertung von Oberflächenrissen. Berlin: Springer; 1984.

[22] El Haddad M, Topper T, Smith K. Prediction of non-propagating cracks. Eng Fract Mech 1979;11:573–84.

[23] Murakami Y. Metal fatigue: effects of small defects and nonmetallic inclusions. Oxford: Elsevier; 2002. p. 88–94.